Wear 368-369 (2016) 219–229

Contents lists available at ScienceDirect

Wear

journal homepage: www.elsevier.com/locate/wear

A study of debris and wear damage resulting from fretting of Incoloy 800 steam generator tubes against AISI Type 304 stainless steel

S.R. Soria [a,b,*], A. Tolley [a,b], A. Yawny [a,b]

[a] División Física de Metales, Centro Atómico Bariloche – Instituto Balseiro, CNEA – Av. E. Bustillo 9500, 8400 S. C. de Bariloche, Argentina
[b] CONICET (Consejo Nacional de Investigaciones Científicas y Técnicas), Argentina

ARTICLE INFO

Article history:
Received 7 September 2016
Accepted 24 September 2016
Available online 29 September 2016

Keywords:
Incoloy 800
Steam generator tubes
Triboparticles
Fretting

ABSTRACT

Wear damage and resulting triboparticles corresponding to fretting of Incoloy 800 steam generator tubes against AISI 304 pads were characterized in experiments performed in air at room temperature in a 90° cross cylinder configuration. Relative displacement amplitudes of 70, 116 and 160 μm under a normal contact load of 35 ± 4 N were considered in experiments performed up to 10^6cycles. The topography and dimensions of the resulting scars on surfaces were characterized using light microscopy and scanning electron microscopy. The morphology, size and crystal structure of the debris detached during the test were determined by transmission electron microscopy and energy dispersive X-ray spectroscopy. It was verified that gross slip was the prevailing running fretting condition in all cases, while the characteristics of the scar surface layer and the corresponding wear mechanisms were found to depend on the amplitude of the relative displacement. Debris consisted in agglomerations of nano-crystalline oxide particles sized between 5 and 20 nm. The crystal structure of debris was found to depend on the displacement amplitude. For 70 μm and 116 μm, NiO, $(Fe,Cr)_2O_3$ and $(Ni,Fe)(Fe,Cr)_2O_4$ were found, while the formation of $(Fe,Cr_2)O_3$ and $(Ni, Fe)(Fe,Cr)_2O_4$ was verified for a displacement amplitude of 160 μm.

1. Introduction

Steam generators (SGs) are one of the most important components of nuclear power plants. They are large heat exchangers where the heat produced in the reactor core is used to generate water steam to drive the turbines and the electric generators. In the case of the pressurized water reactors or pressurized heavy water reactors (PWRs or PHWRs, respectively), the nuclear heat is transported by the primary water coolant circuit and interchanged in the SG to the water steam secondary system. The majority of the SGs used in the nuclear industry are shell and tube heat exchangers. To maximize the heat transfer efficiency, SGs consist of complex arrangements of several thousands of thin walled steam generator tubes (SGTs) which represent a high percent (> 60%) of the total primary system pressure retaining boundary area [1]. In case of any leakage originated in defects in the tubes, the pressure difference between both water circuits will result in the passage of radioactive containing elements from the primary to the secondary circuit. This constitutes an undesirable situation from the point of view of safety due to the increased risk of radioactive release to the environment. Its remediation requires unscheduled reactor shut offs with the consequent negative economic impact. Therefore, assuring the structural integrity of SGTs is essential for both the safe and efficient operation of a nuclear power plant.

One of the actual relevant degradation mechanisms in SGTs is fretting [1]. Fretting is a complex damage mechanism which takes place between two contacting surfaces where a long term oscillating relative displacement of small amplitude (1–300 μm) exists. In the case of SGTs, it is caused by flow induced vibrations (FIVs) [2] due to secondary coolant cross-flow. FIVs result in relative displacements between SGTs and their supports and anti-vibration plates [1]. Fine oxide wear particles referred to as debris [3] or triboparticles [4] are formed during the process. Due to the small relative displacements involved, most of the debris remains trapped between the contacting surfaces. Fretting involves then the synergistic combination of processes such as abrasion, adhesion and tribochemical reactions between the particles and the interacting surfaces [5]. The size, composition and crystal structure of the debris determine the severity of the induced damage on the components in contact. Indeed, it has been demonstrated that the presence of an oxide layer is beneficial while the formation of hard oxides particles is detrimental concerning the severity of the induced damage [6,7].

Studies about the relationship between triboparticles and the resulting fretting damage have been performed by several authors

* Corresponding author at: División Física de Metales, Centro Atómico Bariloche – Instituto Balseiro, CNEA – Av. E. Bustillo 9500, 8400 S. C. de Bariloche, Argentina.

http://dx.doi.org/10.1016/j.wear.2016.09.022
0043-1648/

on a few Ni based alloys and on steels [4,6–8]. Also, some other studies have focussed on the formation of a protective oxide compact glazed layer in Fe and Ni based alloys [9–11]. Incoloy 800 is a Fe-Ni based material characterized by an excellent corrosion resistance and adequate mechanical properties in water and steam media at temperatures near 300 °C [12]. It is already used in the fabrication of SGs and it is also a candidate material in some of the new reactor designs. However, detailed characterization of damage and triboparticles produced in fretting of Incoloy 800 against AISI 304 stainless steel are lacking. It has been shown [3,13] that the composition and microstructure of the materials in contact are important factors in the fretting process. Therefore, a detailed investigation of this system is relevant. In particular, the study of debris can provide valuable information to better understand the complex mechanisms involved during the fretting process. Previous studies on the fretting behaviour of Incoloy 800 and other superalloys used in SGTs have focussed mainly on the effect of different environments and loading conditions on the damage severity characterized by the removed wear volume and the acting wear mechanism [14–17]. In the present work, fretting wear between Incoloy 800 SGTs in contact with AISI 304 stainless steel pads is addressed. Considering the important role of the oxide triboparticles in the mechanisms of fretting, a detailed characterization of the structure of triboparticles and the compact oxide layers formed on the wear surfaces was carried out in order to analyze the observed wear damage.

2. Materials and methods

Fretting tests were realized in SGTs of Incoloy 800 (I 800) with 15.87 mm diameter and 1.13 mm wall thickness. The support plates were simulated using AISI Type 304 stainless steel solid semi-cylindrical pads with a diameter of 13.5 mm in 90° cross cylinder geometry. The nominal composition of the materials used is presented in Table 1. The basic room temperature mechanical properties of the Incoloy 800 SGTs were determined by tensile testing full-size tubular specimens with snug-fitting metal plugs inserts at both ends of the specimen for proper gripping. The obtained results are given in Table 2 where the nominal mechanical properties of AISI 304 pads according to ASTM A276 [18] were also included. Additionally, Vickers Hardness (HV) on the external surfaces of both Incoloy 800 tube and AISI 304 pad was determined using a Mitutoyo MKV-H0 hardness tester using a load of 0.3 kgf (Table 2).

For the fretting tests, an in-house designed testing rig was employed. It consists of an elastic cantilever beam mounted in a MTS 810 servo-hydraulic testing machine as shown in Fig. 1. The SGT tube was gripped in the vertical direction to the mobile piston using the bottom hydraulic grip shown in the Fig. 1. The AISI 304 semi cylindrical pad counterpart was fixed in a 90° cross cylinder configuration to the cantilever beam at a pre-calibrated distance, according to the desired normal contact load. Tests were performed in air at room temperature (25 °C, 35% relative humidity). Although these are not the operating conditions, the room temperature, dry air environment is a convenient first step in tackling the problem. Normal load F adopted for the experiments was of 35 N. This value was selected as a representative load following the recent work concerning fluidelastic forces and fretting wear of steam generators tubes [19]. The maximum error in the normal force was estimated at $\pm$ 4 N, considering the combined effect of the uncertainty in positioning the pad along the elastic beam and the load change that might occur during the test due to the small variation in beam deflection associated with the development of the scar. The displacement amplitudes δ chosen for the present study were of 70, 116 and 160 μm. The associated error was $\pm$ 2 μm. In all cases the imposed displacement was sinusoidal with a frequency 15 Hz and tests were conducted up to a total of 10^6 cycles. According to the geometry illustrated in Fig. 1, the direction of the imposed relative displacement was coincident with the longitudinal direction of the SGTs and transversal to the longitudinal direction of the semi cylindrical pads.

The characterization of the resulting surface damage after 10^6 cycles on both SGT and pad was performed using a Leica DMR Light Microscope (LM) and a Phillips 515 Scanning Electron Microscope (SEM). This was done in two stages. First, the scar area was studied keeping the surface conditions as close as possible to those representing the actual situation after testing. In a second stage, the specimens were rinsed using an ultrasonic bath with acetone and ethanol in order to remove debris and loosely adhered surface layers before reanalyzing them. In addition, the depth of the scar was measured using a Wyco NTC1100 optical profiler.

Debris that detached from the interacting surfaces during the fretting experiments were characterized using the following

Table 1
Nominal composition of the Incoloy 800 and AISI Type 304 steel (wt%).

Material	Fe	Ni	Cr	Cu	C	Mn	S	Si
I 800	42.2	33	21.6	0.09	0.017	0.55	0.003	0.54
AISI 304	66.6 min	8–11	18–20	–	0.08	2	0.003	1

Table 2
Basic mechanical properties of Incoloy 800 SGT and AISI Type 304 pad.

	0.2% Yield Strength	Tensile Strength	Strain to fracture	Young's Modulus	Vickers Hardness
I 800	260 MPa	590 MPa	46%	196 GPa	215 ± 22
AISI 304	205 MPa	515 MPa	40%	193–200 GPa	321 ± 23

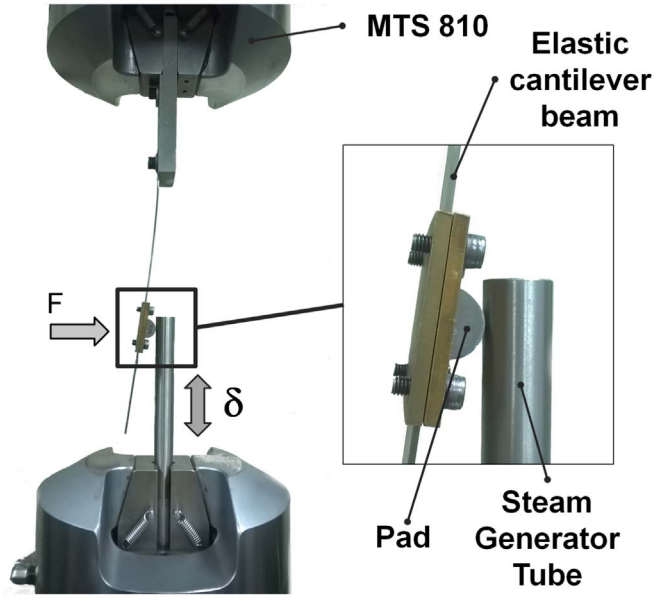

Fig. 1. Fretting wear test rig used.

procedure. Firstly, a clean paper cup was used to collect the debris falling from the contact area along the test. The collected particles were then mixed with ethanol to obtain a colloidal suspension into which a Cu grid with Formvar/Carbon film was immersed. Particles attached to the film after removing it from the suspension were studied in a Philips CM200 Transmission Electron Microscope (TEM) equipped with a LaB_6 cathode, an Ultratwin lens and an EDAX energy dispersive X-ray (EDS) microanalyser, operated at 200 kV.

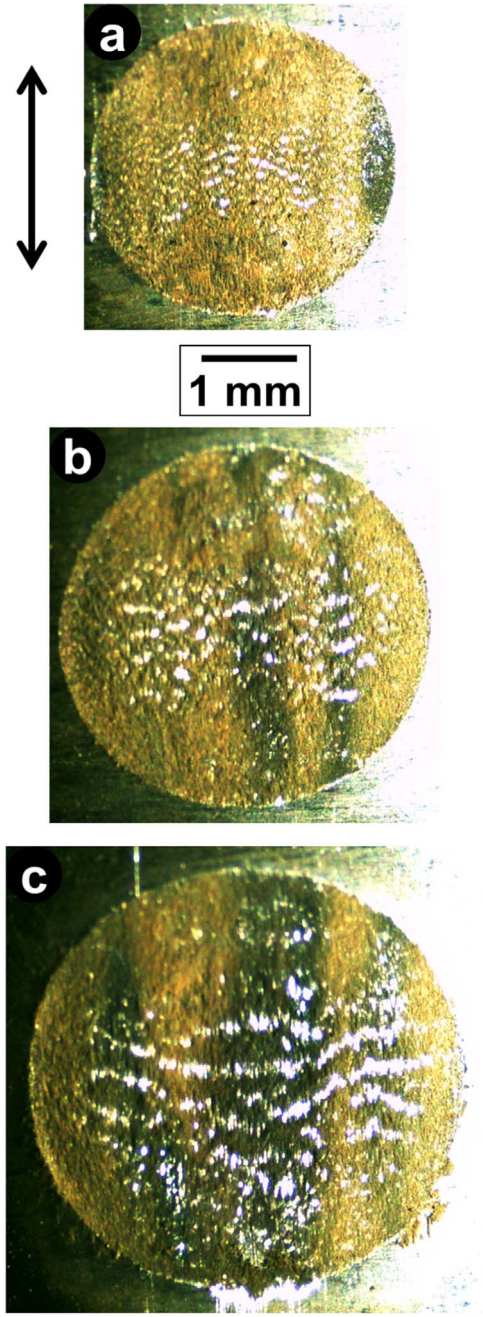

Fig. 2. LM images of fretting scars produced in I 800 SGTs for (a) $\delta = 70$ μm, (b) $\delta = 1$ μm and (c) $\delta = 160$ μm. Arrows indicate the displacement direction.

Table 3
Average scar diameter D in SGT and pad for displacement amplitudes $\delta = 70$ μm, 116 μm and 160 μm.

D [mm]	$\delta = 70$ μm	$\delta = 116$ μm	$\delta = 160$ μm
SGT	3.12	3.84	4.48
Pad	3.10	3.78	4.31

3. Results and discussion

3.1. Evolution of the surface damage

The general topographic characteristics of the scars produced in the SGTs after the ultrasonic cleaning can be appreciated from the LM images presented in Fig. 2. The displacement direction is indicated by the horizontal black arrows. It can be seen that the scars present a circular shape, typical of the 90° cross cylinder geometry used in the tests. In all cases, analysis of the LM images indicates the presence of sliding marks over the entire surface of the scars. The absence of a central zone without wear marks aligned in the displacement direction suggests that gross slip is the dominant fretting running condition in the present experiments. This is in line with the conclusions arrived at by Hurricks [3] and Vingsbo and Söderberg [20] in previous studies with different material pairs.

Applying ImageJ 1.46 image analysis software [21] to the LM micrographs shown in Fig. 2, the average scar diameter D was evaluated from the scar area A and perimeter P [22] of the individual scars using the expression:

Table 4
Calculated volume of removed material and scar in SGTs and pads for different δ together with the scar depth measured with optical profiler in the AISI 304 pads and volume of removed material.

	$\delta = 70$ μm	$\delta = 116$ μm	$\delta = 160$ μm
h_{SGT} [μm]	155	237	325
V_{SGT} [mm^3]	0.59	1.38	2.58
h_{PAD} [μm]	181	270	353
V_{PAD} [mm^3]	0.69	1.52	2.60
h_{PAD}^{OP} [μm]	92	108	118
V_{PAD}^{OP} [mm^3]	0.62	0.84	1.07

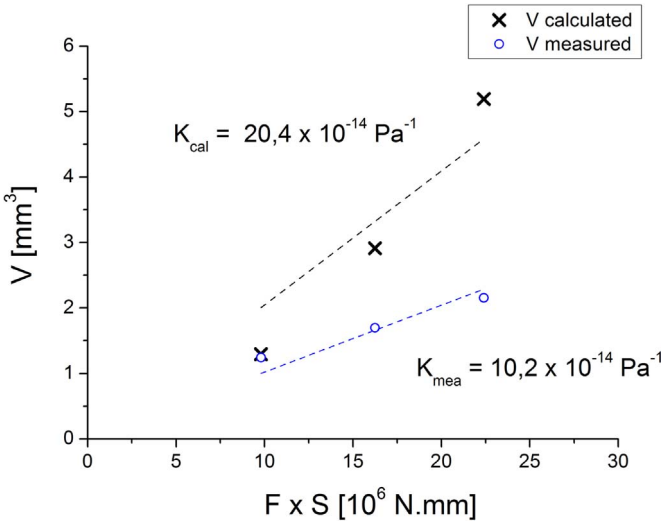

Fig. 3. Determination of Archard wear coefficient K calculated with the spherical cap model (K_{cal}) and the measured depth profile (K_{mea}) for the I 800/AISI 304 pair.

$$D = \frac{4 \cdot A}{P} \tag{1}$$

The results, presented in Table 3, indicate that an increase of displacement amplitude leads to an increase of the scar size.

The maximum depth of the scar h and the volume of material removed V_r were estimated from the average values of the scar diameter D of the pads and SGTs (Table 3), following the ASTM G-204 standard test recommendations [23]. Eqs. (2) and (3) were used. These equations assume contact between a flat surface and a spherical surface of radius r. As in the present work the contact corresponded to 90° crossed cylindrical surfaces, r is taken to be the radius of the SGT or the pad, respectively.

$$h = r - \left[r^2 - \frac{D^2}{4} \right]^{1/2} \tag{2}$$

$$V_r = \frac{\pi h}{6} \left[h^2 - \frac{3D^2}{4} \right] \tag{3}$$

The results of the calculated maximum depth h and the volume of removed material Vr for SGT (h_{SGT}, V_{SGT}) and pad (h_{PAD}, V_{PAD}) are given in Table 4. These results together with those presented in Table 3 indicate that the volume of material removed increases with the displacement amplitude. This effect is characteristic of gross slip situations as was explained in [20].

The total wear volume V, defined as the sum of the volumes V_{SGT} and V_{PAD} of material removed in the SGT and the pad, was used to calculate the fretting wear coefficient K (in Pa^{-1}) using Eq. (4) proposed by Archard [24]. Here F is the applied normal load and S is the total displacement distance that is calculated from the displacement amplitude δ and the number of cycles N:

$$V = K \cdot F \cdot S \Rightarrow K = \frac{V}{F \cdot S} = \frac{V}{F \cdot 4 \cdot \delta \cdot N} \tag{4}$$

The wear coefficient for the I 800/AISI 304 pair was calculated by plotting the total wear volume V against the product $F \cdot S$. Assuming Eq. (4) is valid, a straight line through the origin was fitted to the data. The wear coefficient thus obtained was $K_{cal} = 20.4 \times 10^{-14}\ Pa^{-1}$ as shown in Fig. 3. This value is similar to reported wear coefficient for Inconel 690 and Inconel 600 in contact with AISI 304 stainless steel at room temperature and normal load conditions in the gross slip regime [25].

In order to validate the above mentioned calculations, the depth profiles along the middle line of the pad´s scars were measured using an optical profiler. The scars of the pads were chosen because they are deeper and therefore the experimental errors in the depth measurements are smaller. Due to the size of

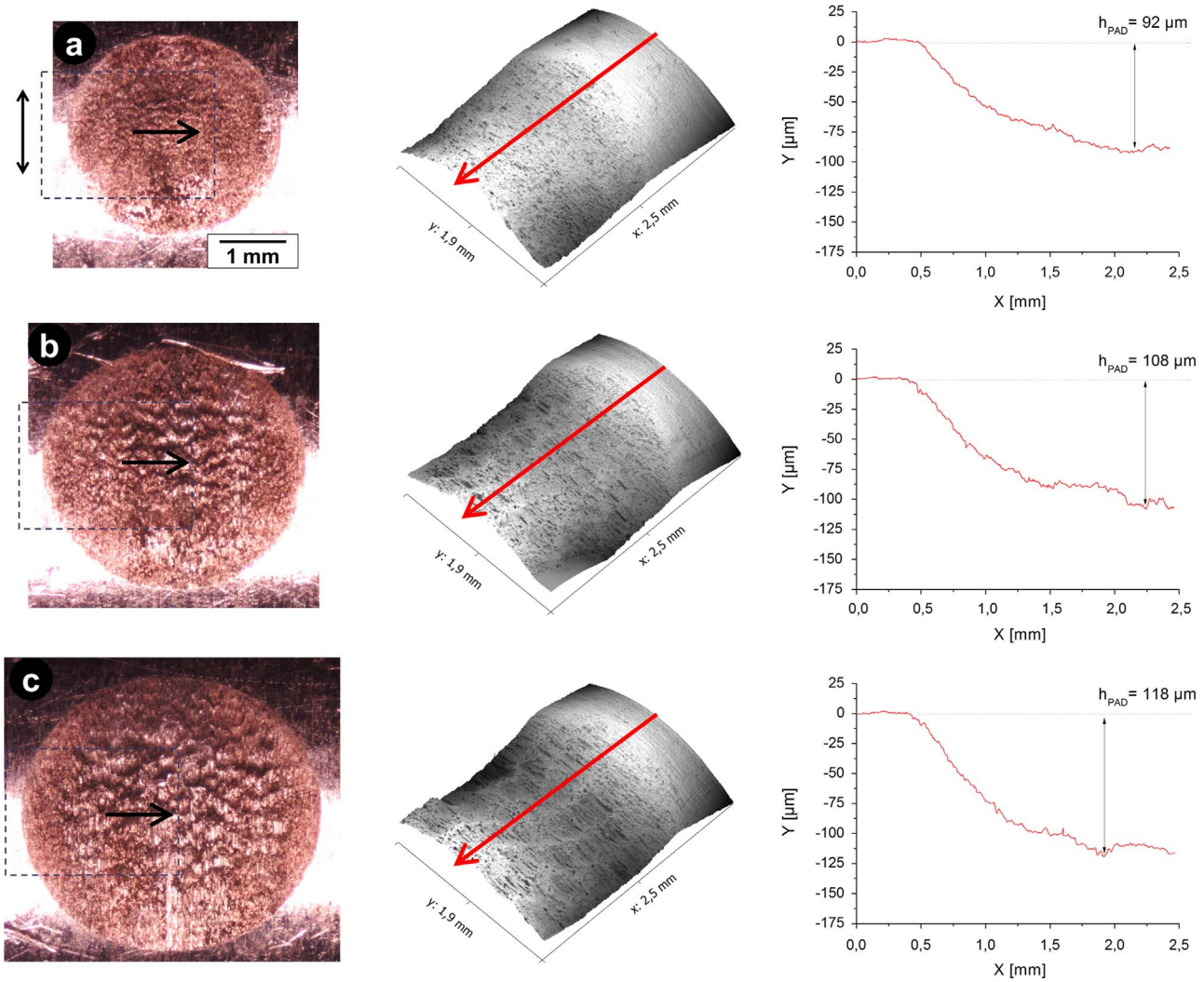

Fig. 4. LM images (left), surface topography (center) and central profile of scars on AISI 304 pads (right) for (a) $\delta = 70$ µm, (b) $\delta = 116$ µm and (c) $\delta = 160$ µm.

the scars, only one half of the profile was determined for the different displacement amplitudes studied. The results are presented in Fig. 4. The maximum depths determined were $h_{PAD}^{OP} = 92, 108$ and 118 μm for δ of 70, 116 and 160 μm, respectively (Table 4). An increase in maximum depth of the scar with increasing displacement amplitude was observed, which is expected for gross slip conditions in fretting [20]. Similar effects have been recently reported due to increasing number of cycles at a fixed displacement amplitude in gross slip conditions in Inconel 600 against AISI 304 [14]. Comparing the calculated and measured values of the maximum depth, it is clear that the calculations based on the spherical cap assumption overestimate the maximum depth. The measured profiles deviate from that of a spherical cap and this deviation increases with displacement amplitude. These results support previous observations of De Baets et al. [26] who reported that the assumption of a spherical cap strongly overrates the real wear volumes.

Based on the previous considerations it was decided to estimate the total volume of removed material V as twice the volume of material removed from the pads V_{PAD}^{OP} calculated now by integrating the experimental depth information provided by optical profilometry. Using these values, a more trustworthy wear coefficient was obtained of $K_{mea} = 10.2 \times 10^{-14}\ \mathrm{Pa}^{-1}$ (Fig. 3).

Analysis of the SEM micrographs of the SGTs scar surface obtained before the ultrasonic cleaning indicates the presence of triboparticles for the three displacement amplitudes considered as shown in Fig. 5(a), (c) and (e). It can be seen that some of the particles remain firmly adhered to the scar surface contributing to the formation of a compacted-debris surface layer. Other particles remain loosely attached to the worn surface. The size and area density of the particles increases with increasing displacement amplitude.

In addition, SEM micrographs representative of the scar surface obtained after rinsing the specimens in ultrasonic bath are presented in Fig. 5(b), (d) and (f). Although in all cases the material tribo pairs exhibited typical characteristics of the gross slip regime, the topographical details of the oxide surface layer formed were found to depend on the magnitude of the relative displacements. This can be explained by considering that most of the generated debris remains trapped in the contact zone between the two interacting materials. There, they suffer oxidation, deformation, and fragmentation into smaller debris particles which in turn

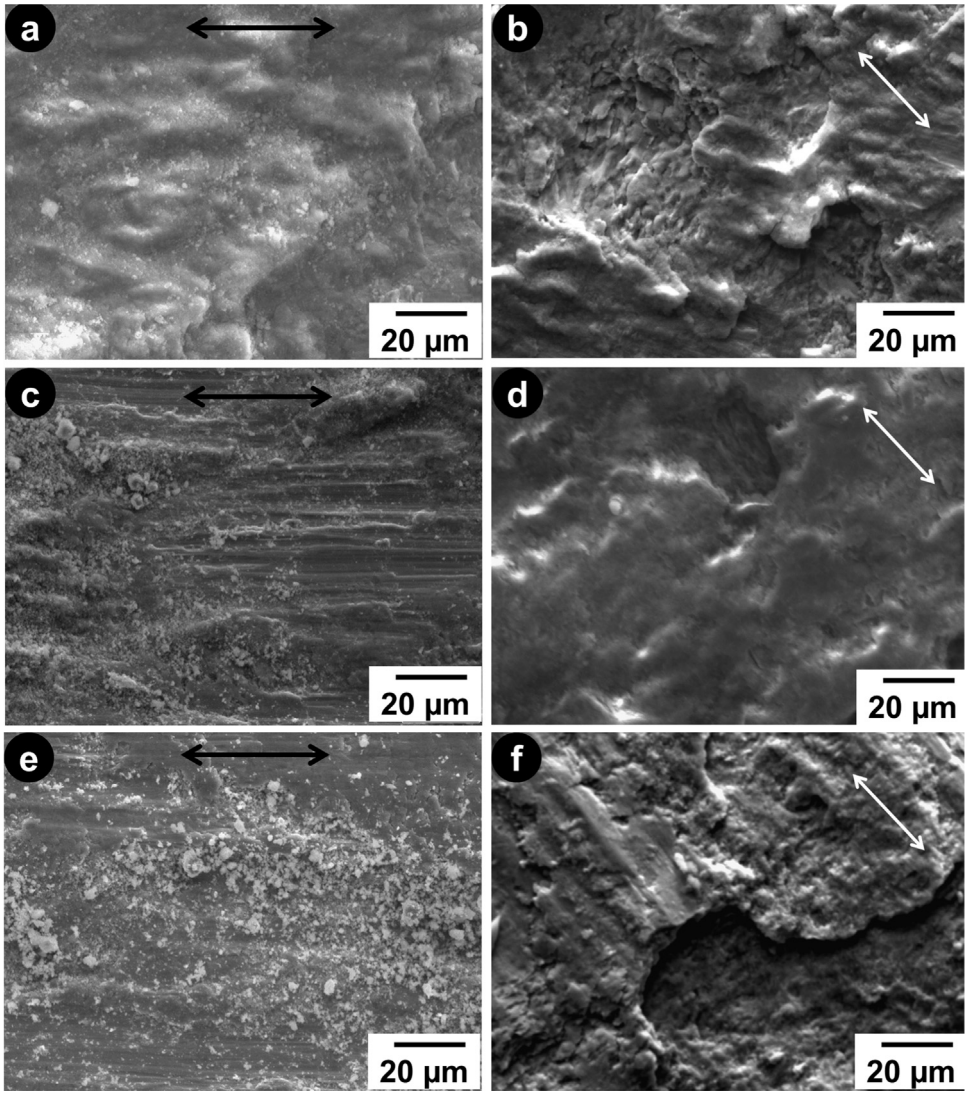

Fig. 5. SEM images of scars on I 800 before ultrasonic cleaning for (a) $\delta = 70$ μm, (c) $\delta = 116$ μm and (e) $\delta = 160$ μm and after cleaning for (b) $\delta = 70$ μm, (e) $\delta = 116$ μm and (f) $\delta = 160$ μm. Arrows indicate the displacement direction.

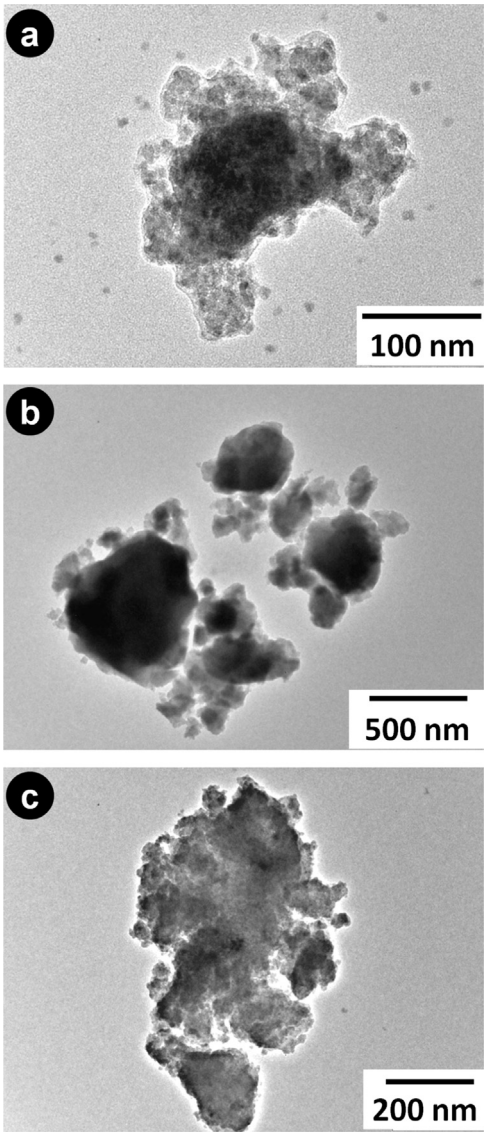

Fig. 6. TEM images of debris corresponding to (a) $\delta = 70$ μm, (b) $\delta = 116$ μm and (c) $\delta = 160$ μm.

agglomerate and are compacted to constitute the so-called compact oxide surface layer. Under particular conditions of load, temperature and displacement velocity, they might transform into the so-called glazed layer [27]. Glazes are assumed to be protective oxide layers which are formed by the compaction and sintering of the individual particles due to the local temperature increase and high pressures involved. It is important to remark here that these layers are referred to as glazed layers because they exhibit a glassy appearance but in fact they are thin polycrystalline layers [10].

From the analysis of the observed characteristics of the compact oxide layer formed at the different displacement amplitudes, the following situations were identified, based on the studies of Pauchwithz et al. [27]:

(i) Condition of "no layer" formation (NL). For $\delta = 70$ μm, low adherence between the compact debris and the metal surface resulted in total delamination during ultrasonic cleaning, as shown in Fig. 5(b). Marks formed during delamination can be seen.
(ii) The mechanically mixed layer (MML) formation. For $\delta = 116$

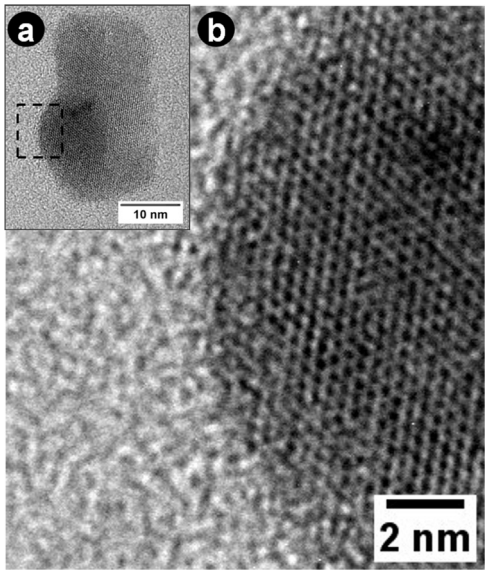

Fig. 7. Isolated particle from detached debris for $\delta = 70$ μm. (a) Bright Field image; (b) HRTEM image of the area indicated in (a).

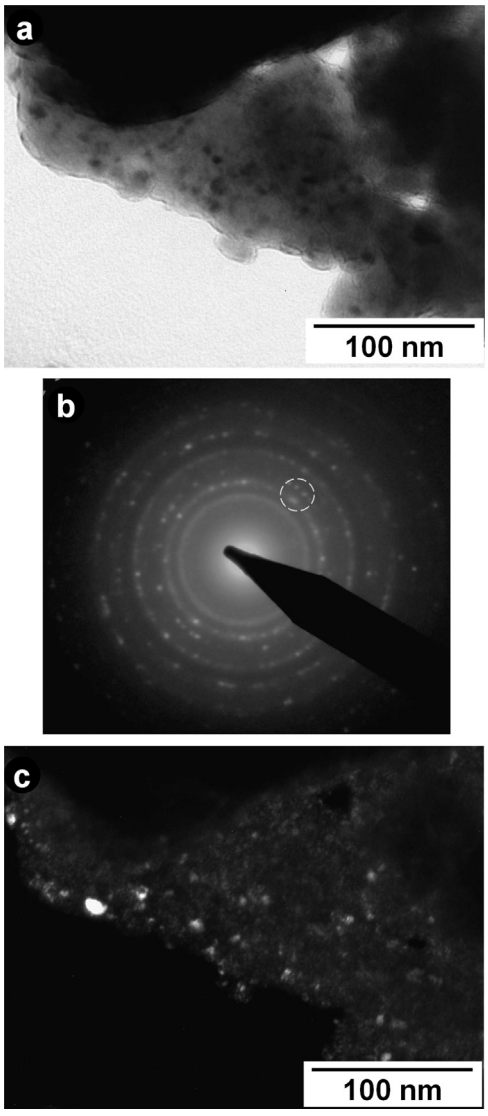

Fig. 8. TEM images of debris corresponding to $\delta = 116$ μm. (a) Bright Field image, (b) EDP and (c) Dark Field image.

μm, the surface shows a layer with a smoother appearance than the original surface of SGT as shown in Fig. 5(d) that results from the high compaction of the debris which then remained adhered to the SGT. Its formation required a temperature above room temperature. Roughness of this layer decreases with an increase of the contact zone temperature.

(iii) The Composite Layer (CL) formation. For $\delta = 160$ μm, a glaze layer was observed as shown in Fig. 5(f). The surface features indicate the beginning of a sintering process originated by the combined effect of the increase of pressure in debris compaction and the increase of temperature due to friction. Small abrasion grooves in the displacement direction are observed together with partial detachment of the layer. Such grooves indicate the presence of abrasion processes originated by hard particles.

The observation of the center of the contact surface by LM in Fig. 2 reveals the formation of ripples normal to the sliding direction on SGTs surface. The presence of ripples or surface waves have been reported in recent studies of tangential fretting [28,29], which were attributed to the individual interlocking pairs of surface bumps (protruding materials) and depressions caused by the fretting wear. However, those authors did not consider the influence of the compliance of the test rig and its effects on the size and characteristics of the fretting wear scars.

On the other hand, the formation of ripples was reported in rotational fretting experiments in polymers [30]. During the early cycles flake like debris accumulate in the center of the scar because in this zone the direction of the relative movement is reversed and the presence of stick and slip zones generates thin ripples. As the test proceeds, the size of the ripples and the distance between them increase due to an increase of load on the ripples by the reduction of the real contact area, favoring the flip-flop movement in the central zone [31] and giving the ripples their characteristics shape.

In tangential fretting with micrometer displacements, a combined mode of sliding and rolling is present if angular displacements of a few degrees exist in the presence of vibrations [32]. In the test rig used in the present work, a bending moment is present, originated in the elastic cantilever on the contact zone between pad and SGT beam due to the friction force. This leads to a combined mode of tangential and rotational fretting that might also be the responsible of ripples in the center of scar.

3.2. Debris characterization

TEM characterization of the detached debris indicates the presence of isolated particles with sizes between 5 and 20 nm, together with larger sized particles with sizes between 100 nm and 500 nm as shown in Fig. 6. The isolated nanoparticles presented a crystalline contrast under High Resolution TEM (HRTEM) as can be seen in the image shown in Fig. 7.

The larger particles shown in Fig. 6 were found to be agglomerates of small crystallites or grains. This is illustrated in Fig. 8 where results for debris obtained for $\delta = 116$ μm are shown. The electron diffraction pattern obtained from a large particle of the debris, shown in Fig. 8(a), can be seen in Fig. 8(b). It consists of concentric rings of reflections indicating that the large particles are a collection of randomly oriented small crystallites or grains. A Dark Field Image formed by selecting a portion of the diffracted rings indicated in Fig. 8(b), shown in Fig. 8(c), indicates that the sizes of the crystallites is between 5 and 20 nm.

The local composition within debris particles was determined by EDS spectroscopy, using an electron beam with a size around

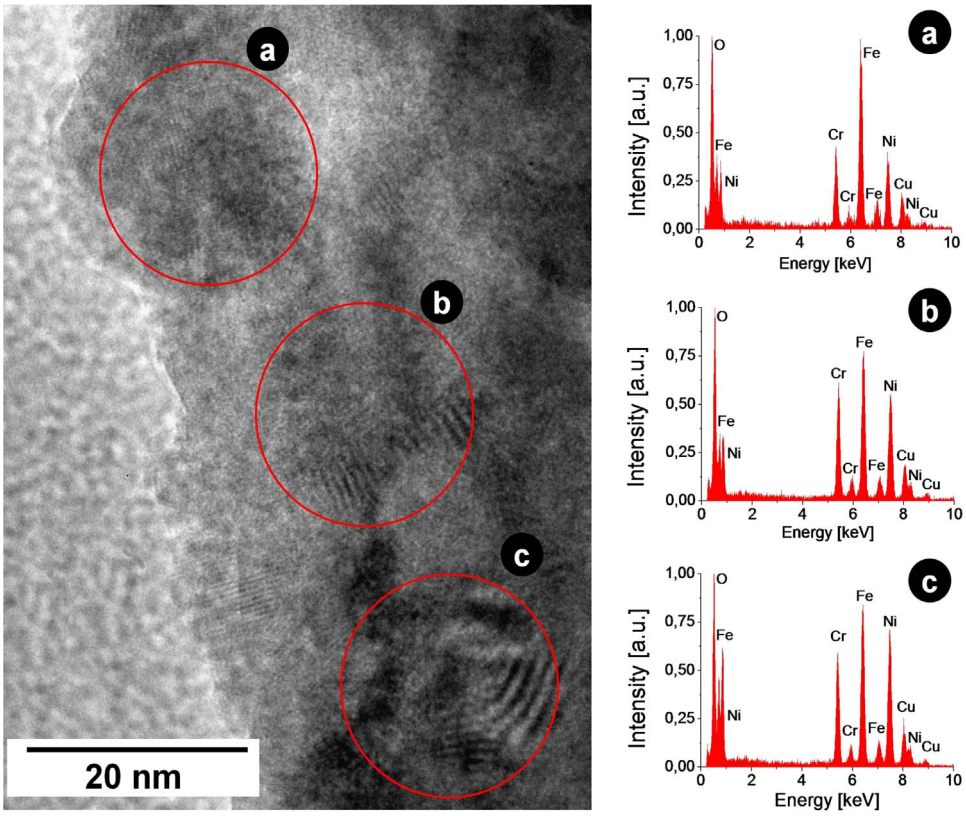

Fig. 9. TEM image and corresponding EDS spectra for different position on the same debris for $\delta = 116$ μm.

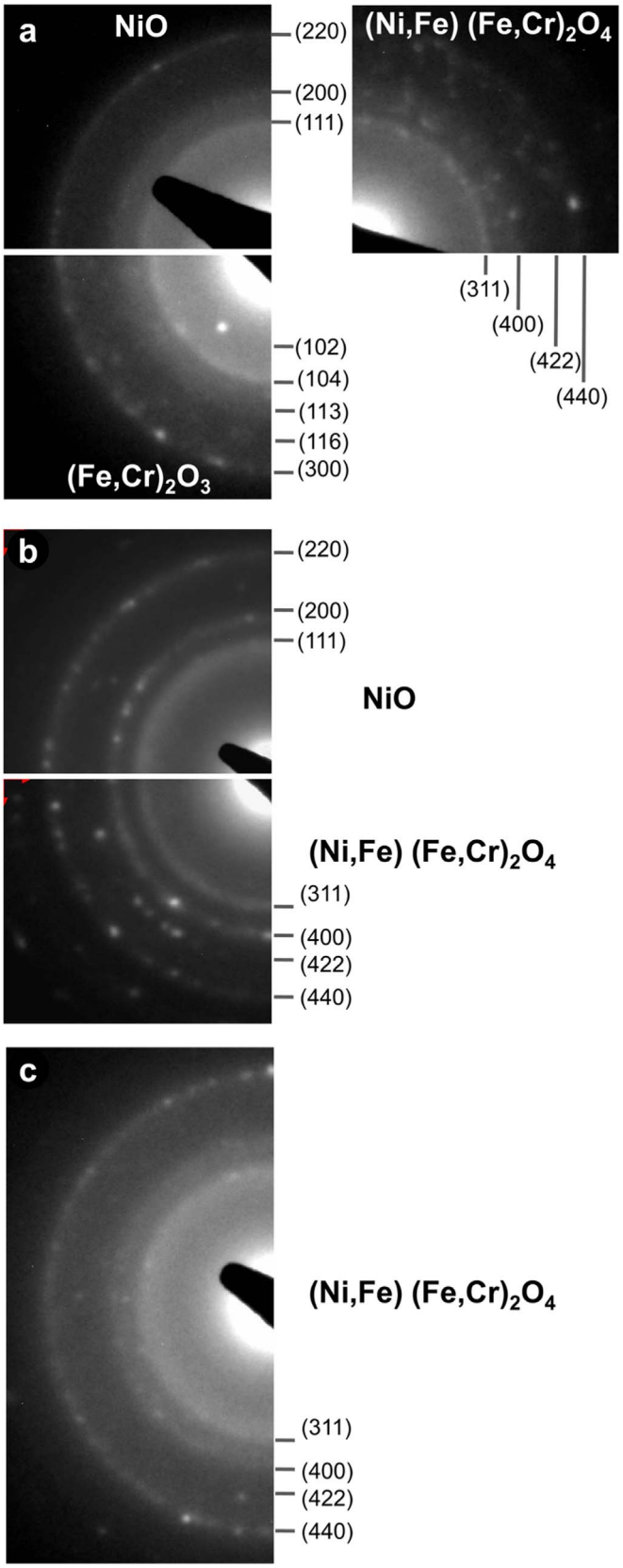

Fig. 10. Characterization of the debris crystalline structure by TEM corresponding to (a) $\delta = 70$ μm, (b) $\delta = 116$ μm and (c) $\delta = 160$ μm.

20 nm. Fig. 9 shows the results obtained in several nearby regions of a particle. The presence of Fe, Cr and Ni was detected in all regions, but the peak intensity was found to vary from region to region, indicating that debris have an inhomogeneous composition. In the EDS spectra shown in Fig. 9, the Cu peak corresponds to spurious X-rays from the support grid.

Typical Electron Diffraction Patterns (EDPs) of large debris particles such as that in Fig. 8(b), consist of numerous rings of reflections that correspond to a superposition of different phases. In all the cases studied, more than one phase was observed in the debris. In order to separate out individual phases, small regions of sizes between 100 and 200 nm were analyzed combining EDP analysis with EDS spectroscopy. The analysis of the ring diffraction patterns together with the EDS spectra showed that the phases present were non-stoichiometric complex oxides of the principal elements (Fe, Ni and Cr) with spinel and hematite type structures. In these oxides, Fe^{2+} and Ni^{2+} ions occupy tetrahedral sites while Fe^{3+} and Cr^{3+} ions occupy octahedral sites, leading to local variations of composition observed in the EDS spectra.

Fig. 10 illustrates the results of the phase identification combining EDP analysis with EDS spectra. For $\delta = 70$ μm the phases were NiO and $(Ni,Fe)(Fe,Cr)_2O_4$ spinel, together with a weak ring of a modified $(Fe,Cr)_2O_3$ hematite where partial substitution of Fe by Cr takes place. For $\delta = 116$ μm, rings corresponding to NiO and $(Ni,Fe)(Fe,Cr)_2O_4$ were identified and reflections compatible with interplanar spacings of $(Fe,Cr)_2O_3$ were also found. Finally, for $\delta = 160$ μm rings corresponding to $(Ni,Fe)(Fe,Cr)_2O_4$ were present, and larger spacings compatible with $(Fe,Cr)_2O_3$ were again observed. The presence of small particles with modified $(Fe,Cr)_2O_3$ hematite structure in the debris corresponding to displacement amplitudes of 116 μm and 160 μm was confirmed by High Resolution Imaging. In Fig. 11, lattice fringes of small crystallites and their diffractograms obtained by Fast Fourier Processing with a spacing corresponding to the 102 reflection are shown.

The formation of non-stoichiometric oxides of spinel and hematite structures has been studied in relation with corrosion effects in aqueous environments at temperatures near to 300 °C in AISI 304 [33] and Incoloy 800 [34]. In these reports, the formation of two oxide layers with variable stoichiometry was observed. However, the detailed mechanisms for the formation of such structures are not yet completely established.

Formation of spinel phases is not unexpected. Indeed, Fe based spinels, called ferrites and used commonly in magnetic applications, are usually fabricated by high temperature mechanical milling from precursor oxides such as an oxide of the bivalent metallic ion and Fe_2O_3 [35]. The fretting process in which the particles detached remain between the surfaces in contact and suffer plastic shear deformation together with an increase in temperature due to friction is expected to cause the formation of spinels by their similarity with mechanical milling.

The formation of $(Ni,Fe)(Fe,Cr)_2O_4$ spinel at a $\delta = 160$ μm is an important result. A glaze layer with this structure has been reported in studies of sliding wear in Incoloy 800 H and Incoloy 901 at temperatures near to 600 °C [9–11]. The presence of this spinel could therefore explain the formation of a glaze layer for displacement amplitude of 160 μm in the present work. However, the fretting tests were carried out at room temperature, so the increase in temperature to attain glaze layer formation can only be due to frictional heat. The local temperature increase in fretting contact due to frictional power dissipation has been studied recently by finite element simulations [36]. The oxide debris layer was reported to favour this effect [37]. Furthermore, computer simulations in AISI 304 have shown that temperatures around 700 °C can be achieved at the contact point [38]. Such simulations considered the variations of the mechanical and thermal properties in the material with the increase of local temperature. Furthermore, according to the work of Inman et al., a very high hardness of around 1800 HV at 750 °C was measured in a glaze layer of $NiCr_2O_4$ [10], which can lead to a protective effect.

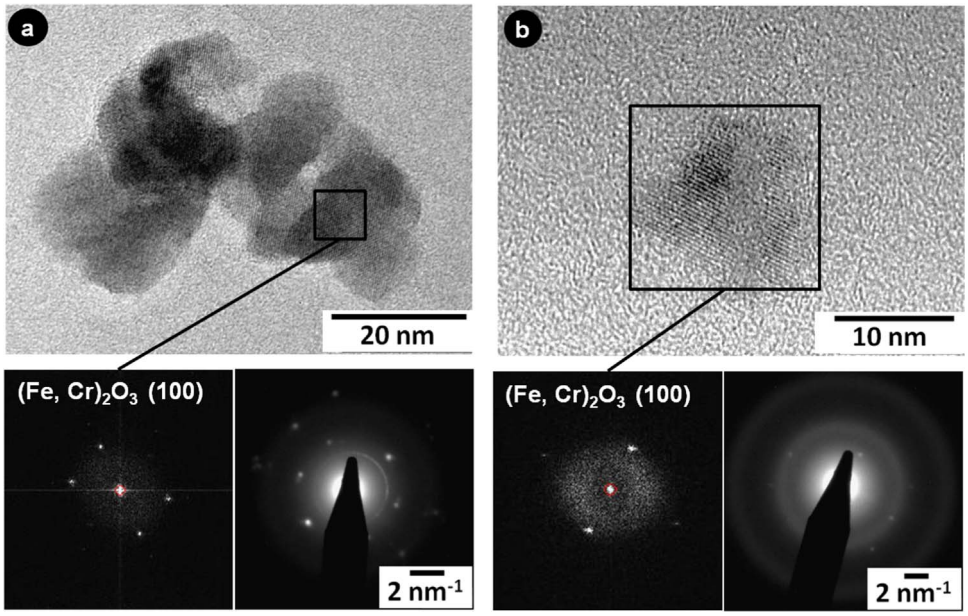

Fig. 11. Nanoparticles of $(Fe,Cr)_2O_3$ by TEM corresponding to (a) $\delta = 116$ μm and (b) $\delta = 160$ μm.

Since the debris was collected during the entire fretting test, it contains particles detached at different stages of the fretting process. During the early stages, the debris particles are simply oxides of the elements of the materials in contact. As the test advances, loose material is retained and compressed between the surfaces forming oxide compact layers. In the final stages debris particles are detached from such layers. Therefore, it can be assumed that the crystalline structure of detached debris is similar to that of the compact layer. This assumption is supported by a recent study of the compact layer formed during fretting tests on Inconel 690 [17] that reported the presence of $NiCr_2O_4$ and Fe_2O_3 on the worn surfaces with an average grain size of 8.5 nm, similar to the results found in the present work.

3.3. Effects of debris on the main wear mechanism

The analysis of scars in the SGTs and pads indicates the presence of different wear mechanisms (Fig. 12). At all displacement amplitudes the presence of grooves due to third body abrasion has been the main wear mechanism. The third bodies were the debris retained between both surfaces, causing grooves through microcutting and microploughing processes [39]. On the other hand, the presence of pits and regions where material transfer was identified is evidence of adhesive wear in conjunction with abrasive wear.

The oxide particles that constitute the debris originated in the fretting process are formed by chemical reactions favored by the particular conditions in the contact area of the interacting bodies. These are called tribochemical reactions because the driving forces are associated with the local temperature and pressure increments and with the agglomeration and breakdown of debris during tests. The importance of tribochemical reactions in gross slip regime was described in a work of Kalin and Vizintin [40]. These authors demonstrated that the tribochemical wear increases with displacement amplitude in gross slip regime.

Predominance of abrasive wear can be explained based on the phases in contact during the tests. In austenitic steels with more than 17 wt% Cr, it has been reported that a duplex protective later was formed on the surface in contact with air. It is composed by an external layer of $(Mn,Fe)Cr_2O_4$ spinel and internal layer of chromium oxide Cr_2O_3 [41]. The latter is a hard phase with around 400 HV in layers of 400 μm in thickness [42]. In the I 800/AISI 304 pair this phase is expected to form in both surfaces due to the high Cr content or due to tribochemical reactions [43] during the fretting process, and was indeed observed in the debris. Therefore the predominance of abrasive wear can be attributed to the presence of $(Fe,Cr)_2O_3$.

4. Conclusions

In the present work the fretting wear behavior of Incoloy 800 steam generator tubes against AISI 304 solid pads was studied for displacement amplitudes $\delta = 70, 116$ and 160 μm under a nominal normal load of 35 N, in air at room temperature (25 °C, 35% relative humidity) up to 10^6 cycles. The following conclusions were drawn from the characterization performed:

In all tests, in gross slip regime was found with the formation of different surface layers according to the displacement amplitude. A protective surface layer or glaze layer was formed at the largest displacement amplitude.

The Archard wear coefficient for the I 800/AISI 304 pair, determined from measurements of the scar depth profiles was $K = 10.2 \times 10^{-14}$ Pa^{-1}.

Ripples in the central regions of the scars were observed. They are probably caused by a rolling effect between the tube and pad due the stiffness of cantilever beam used in the test rig.

TEM characterization of detached debris indicated a wide dispersion in their sizes in all tests, ranging between 100 nm and 500 nm. Such debris were shown to be agglomerates of nanocrystalline particles with sizes between 5 and 20 nm which formed due to their retention between the sliding surfaces.

The composition of these agglomerates varied locally, on a length scale of tens of nm, suggesting the formation of non-stoichiometric oxides. Several phases were identified and were found to vary with the displacement amplitude, indicating the presence of tribochemical reactions. In particular, for a displacement amplitude of 160 μm the formation of a composite layer on the surface was related to the presence of (Ni, Fe)$(Fe,Cr)_2O_4$ in the debris, that is one of the structures proposed by other authors to be the

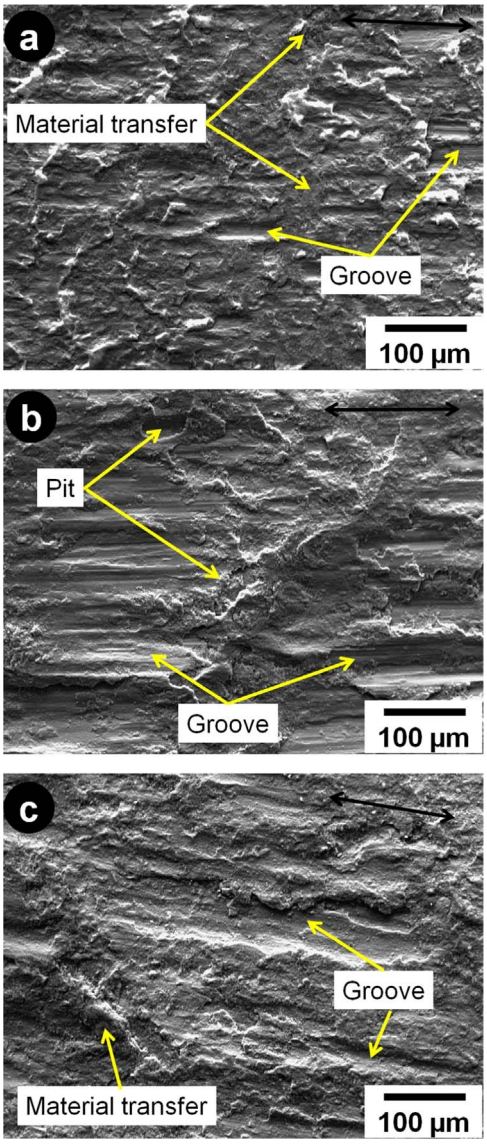

Fig. 12. SEM images of wear surface in AISI 304 pads for (a) $\delta = 70$ μm, (b) $\delta = 116$ μm and (c) $\delta = 160$ μm.

main component of glaze layers in Ni alloys at temperatures near 600 °C.

Adhesive and abrasive wear were observed. They were attributed to the formation of hard oxides between the surfaces during the fretting process.

Acknowledgements

The assistance of Mr. Carlos Cotaro with the SEM observations and of Juan Pablo Balbiani with the fretting tests performed are gratefully acknowledged. We also acknowledge support from ANPCyT (PICT 0898–2011), CONICET and Universidad Nacional de Cuyo.

References

[1] IAEA, TECDOC-1668- Assessment and management of ageing of major nuclear power plant components important to safety: Steam generators, IAEA, Vienna, 2011.
[2] N.J. Fisher, A.B. Chow, M.K. Weckwerth, Experimental fretting-wear studies of steam generator materials, J. Press. Vess. Technol. 117 (1995) 312–320.
[3] P.L. Hurricks, The mechanism of fretting – a review, Wear 15 (1970) 389–409.
[4] J. Jiang, F.H. Stott, M.M. Stack, The role of triboparticulates in dry sliding wear, Tribol. Int. 31 (1998) 245–256.
[5] R.B. Waterhouse, Fretting, Corrosion, Pergamon Press, Oxford, 1972.
[6] F.H. Stott, The role of oxidation in the wear of alloys, Tribol. Int. 31 (1998) 61–71.
[7] J.L. Xuan, H.S. Cheng, Microscopic Wear Debris Generation and Surface Topography, Wear Particles: From the Cradle to the Grave, D. Dowson et al. (Ed.), Elsevier, Amsterdam (1992) 247-256.
[8] J. Wei, S. Fouvry, Ph Kapsa, L. Vincent, Third body effects in fretting, in: D. Dowson, et al., (Eds.), The Third Body Concept, Elsevier, Amsterdam, 1996, pp. 45–53.
[9] F.H. Stott, D.S. Lin, G.C. Wood, The structure and mechanism of formation of the glaze oxide layers produced on Nickel-based alloy during wear at high temperatures, Corros. Sci. 13 (1973) 449–469.
[10] I.A. Inman, P.S. Datta, Studies of high temperature sliding wear of metallic dissimilar interfaces IV: Nimonic 80A versus Incoloy 800HT, Tribol. Int. 44 (2011) 1902–1919.
[11] I.A. Inman, P.S. Datta, Studies of high temperature sliding wear of metallic dissimilar interfaces III: Incoloy MA956 versus Incoloy 800HT, Tribol. Int. 43 (2010) 2051–2071.
[12] Special Metal Corporation, Publication Number SMC-046: INCOLOY® alloy 800 (2004).
[13] J.M. Dobromirski, Variables of fretting process: are there 50 of them?, ASTM STP 1159: standardization of fretting fatigue test, in: M. Helmi Attia, R. B. Waterhouse (Eds.), Methods and Equipment, ASTM, Philadelphia, 1992, pp. 60–66.
[14] J. Li, M. Ma, Y.H. Lu, L. Xin, Evolution of wear damage in Inconel 600 alloy due to fretting against type 304 stainless steel, Wear 346-347 (2016) 15–21.
[15] F.M. Guérout, N.J. Fisher, Steam generator fretting-wear damage: a summary of recent finding, J. Press. Vess. Technol. ASME, 121, 1995, 304-310.
[16] J.K. Hong, I.S. Kim, Environment effects on the reciprocating wear of Incoel690 steam generator tubes, Wear 255 (2003) 1174–1182.
[17] L. Xi, B.B. Yang, Z.H. Wang, J. Li, Y.H. Lu, T. Shoji, Microstructural evolution of subsurface on Inconel 690TT alloy subjected to fretting wear at elevated temperature, Mater. Des. 104 (2016) 152–161.
[18] ASTM A276-2004, Standard Specification for Stainless Steel Bars and Shapes ASTM International, 2004.
[19] M. Hassan, A. Mohany, Simulations of fluidelastic forces and fretting wear in U-bend tube bundles of steam generators: effect of tube-support conditions, in: Proceedings of World Congress Advances in Structural Engineering and Mechanics ASEM 15.
[20] O. Vingsbo, S. Söderberg, On fretting maps, Wear 126 (1988) 131–147.
[21] W.S. Rasband, ImageJ 1.46, http:// rsb.info.nih.gov/ij/.
[22] D.W. Hetzner, Comparing binary image analysis measurements – euclidean geometry, centroids and corners, Microsc. Today 16 (2008) 10.
[23] ASTM G-204, Standard Test Method for Damage to Contacting Solid Surfaces under Fretting Conditions, ASTM International.
[24] J.F. Archard, Contact and rubbing of flat surfaces, J. Appl. Phys. (8) (1953) 981–998.
[25] D.G. Kim, Y.Z. Lee, Experimental investigation on sliding and fretting wear of steam generator tube materials, Wear 250 (2001) 673–680.
[26] P. De Baets, K. Strijckmans, A.P. van Peteghem, Characterization of the fretting wear of unlubricated steel surfaces based on the comparison of wear results obtained by different methods, Wear 208 (1997) 169–176.
[27] A. Pauschitz, M. Roy, F. Franek, Mechanics of sliding wear of metals and alloys at elevated temperatures, Tribol. Int. 41 (2008) 584–602.
[28] D.M. Mulvihill, M.E. Kartal, A.V. Olver, D. Nowell, D.A. Hills, Investigation of non-Coulomb friction behaviour in reciprocating sliding, Wear 271 (2011) 802–816.
[29] J. Hintikka, A. Lehtovaara, A. Mäntylä, Non-Coulomb friction in gross sliding fretting conditions with aluminium bronze against quenched and tempered steel, Tribol. Int. 79 (2014) 151–161.
[30] B.J. Briscoe, A. Chateauminois, T.C. Lindley, D. Parsonage, Fretting wear behaviour of polymethylmethacrylate under linear motions and torsional contact conditions, Tribol. Int. 31 (1998) 701–711.
[31] K.L. Johnson, Contact mechanic, Ch. 8 – Rolling contact of elastic bodies, Cambridge University Press 2003, pp. 243–283.
[32] J.L. Mo, M.H. Zhu, J.F. Zheng, J. Luo, Z.R. Zhou, Study on rotational fretting wear of 7075 aluminum alloy, Tribol. Int. 43 (2010) 912–917.
[33] W. Kuang, E.H. Han, X. Wu, J. Rao, Microstructural characteristics of the oxide scale formed on 304 stainless steel in oxygenated high temperature water, Corros. Sci. 52 (2010) 3654–3660.
[34] B. Stellwag, The mechanics of oxide film formation on austenitic steel in high temperature water, Corros. Sci. 40 (1998) 337–370.
[35] B.D. Cullity, C.D. Graham, Introduction to magnetic materials, Willey, New Jersey, 2009.
[36] X. Jin, P.H. Shipway, W. Sun, The role of frictional power dissipation (as a function of frequency) and test temperature on contact temperature and the subsequent wear behaviour in a stainless steel contact in fretting, Wear 330–331 (2015) 103–111.
[37] X. Jin, W. Sun, P.H. Shipway, The role of geometry changes and debris formation associated with wear on the temperature field in fretting contacts, Tribol. Int. 102 (2016) 392–406.
[38] H.A. Abdel-Aa, A remark on the flash temperature theory, Int. Comm. Heat. Mass Transf. 24 (1997) 241–250.

[39] K. Heinz, Z. Gahr, Microstructure and Wear of Materials, Elsevier, New York, 1987.
[40] M. Kalin, J. Vizintin, A tentative explanation for the tribochemical effects in fretting wear, Wear 250 (2011) 681–689.
[41] C. Ostwald, H.J. Grabke, Initial oxidation and chromium diffusion. I. Effects of surface working on 9–20% Cr steels, Corros. Sci. 46 (2004) 1113.
[42] H. Kitsunai, K. Hokkirigawa, N. Tsumaki, K. Kato, Transitions of microscopic wear mechanism for Cr_2O_3 ceramic coatings during repeated sliding observed in a scanning electron microscope tribosystem, Wear 151 (1991) 279.
[43] N. Kumar, C.R. Das, S. Dash, S.K. Albert, P. Chandramohan, M.P. Srinivasan, A. K. Bhaduri, A.K. Tyagi, B. Raj, Tribo-induced phase transformation and associated evolution of friction of NiCrB Alloy, Tribol. Transactions 55 (2012) 117–121.